Volume 16 | Number 23 | 7 December 2016 | Pages 4469–4630

Lab on a Chip

Miniaturisation for chemistry, physics, biology, materials science and bioengineering

www.rsc.org/loc

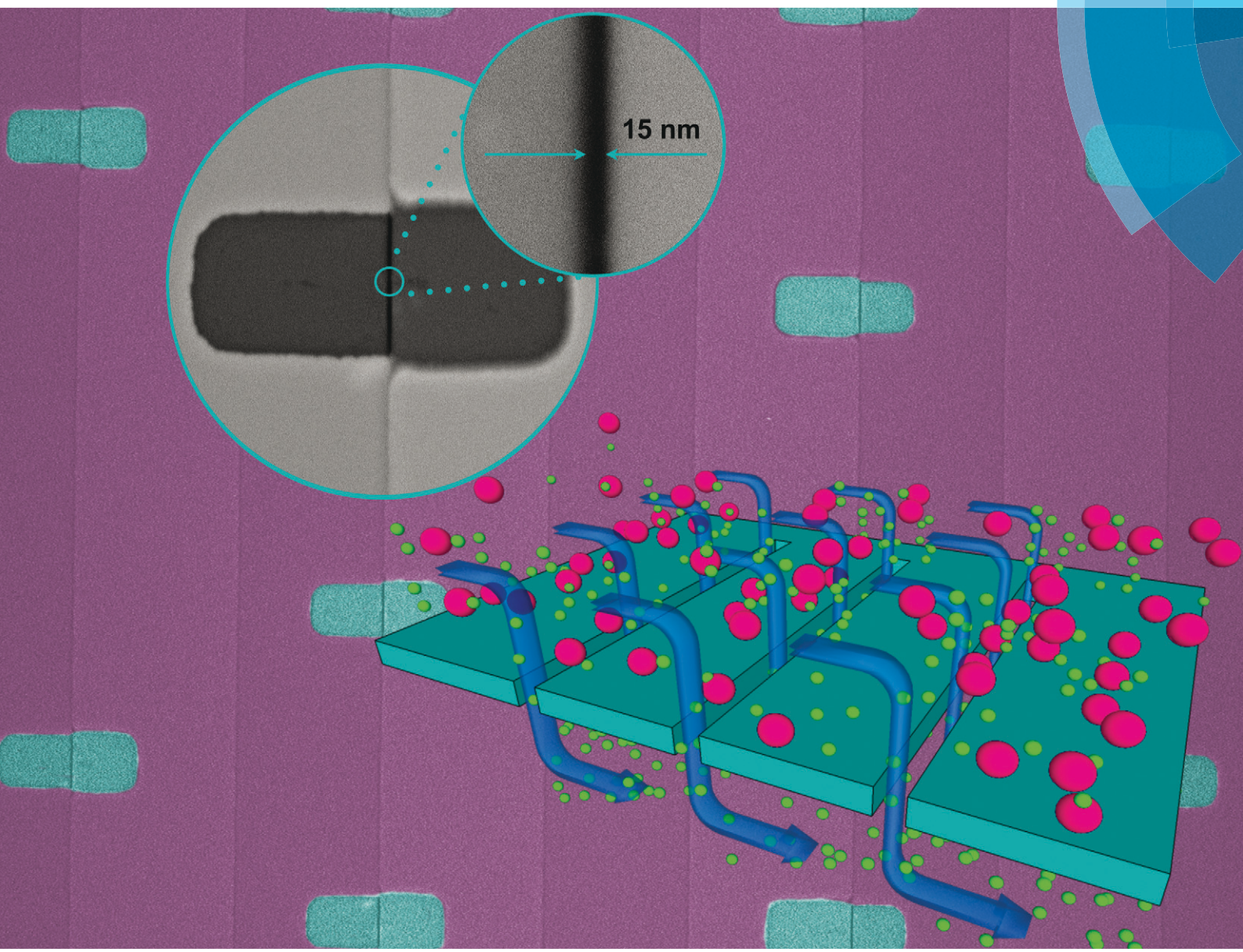

ISSN 1473-0197

ROYAL SOCIETY OF CHEMISTRY

PAPER

Thomas P. Burg *et al.*

Continuous high throughput nanofluidic separation through tangential-flow vertical nanoslit arrays

175 YEARS

Lab on a Chip

PAPER

View Article Online
View Journal | View Issue

Published on 13 October 2016. Downloaded by Stiftung caesar - Bibliothek on 5/12/2020 4:02:52 PM.

Cite this: *Lab Chip*, 2016, **16**, 4546

Continuous high throughput nanofluidic separation through tangential-flow vertical nanoslit arrays†

Margherita Bassu,[a] Peter Holik,[b] Sam Schmitz,[b] Siegfried Steltenkamp[b] and Thomas P. Burg*[a]

Received 29th August 2016,
Accepted 13th October 2016

DOI: 10.1039/c6lc01089j

www.rsc.org/loc

Nanofluidic devices exhibit unique, tunable transport properties that may lead to breakthroughs in molecular separations and sensing. However, the throughput of these devices is orders of magnitude too small for the processing of macroscopic samples. Here we overcome this problem by combining two technological innovations. First, nanofluidic channels are made as vertical slits connecting the two sides of a silicon nitride membrane. Arbitrary arrays of such nanoslits down to 15 nm wide with <6 Å uniformity were made by merging the idea of templating with chemical mechanical polishing to create a scalable, nanolithography-free wafer level process. Second, we provide for efficient solute transport to and from the openings of the nanoslits by incorporating the nanofluidic membrane into a microfluidic tangential-flow system, which is also fabricated at wafer level. As an exemplary application, we demonstrate charge-based continuous flow separation of small molecules with a selectivity of 100 and constant flux over more than 100 hours of operation. This proves the exciting possibility of exploiting transport phenomena governed by precision-engineered nanofluidic devices at a macroscopic scale.

Introduction

Nanofluidic devices are interesting for many applications due to their exceptionally high surface to volume ratio and the unique ability to modulate the permeability to solutes and solvents by physico–chemical interactions at the surface. Our understanding of nanofluidic transport phenomena has grown tremendously over the past ten years, and this has paved the way to exciting new paradigms in the fields of chemical and biological sensing,[1–6] sample preconcentration,[7] molecular separation,[8,9] and water purification.[10] Furthermore, there is the interesting prospect of creating revolutionary new filters by mimicking sophisticated biological transport systems with bio-functionalized arrays of artificial nanopores.[11,12]

Many nanofluidic phenomena exhibit a pronounced size-dependence. Therefore, the fabrication of devices with precise dimensions is an important prerequisite for practical applications. While several current technologies can provide excellent dimensional precision when devices are fabricated one at a time or in small batches, scalability remains a major concern. This is a crucial issue, as most real-world applications require processing of at least a few microliters of liquid while nanofluidic channels typically possess inner volumes on the order of only a few femtoliters. For example, the purification of specific molecules from complex mixtures is only useful if a sufficient quantity can be obtained, and in the field of sensing, large volumes need to be processed whenever the concentration of target molecules is very low.

Scaling up the number of devices without introducing heterogeneity is the key to overcoming the enormous resistance of nanofluidic channels due to their minute hydrodynamic cross section. Furthermore, it is desirable for channels to be not unnecessarily long in order to be able to drive solute and solvent fluxes with low pressure, voltage, chemical potential, or differences in another potential.

Existing technologies for making nanofluidic channels are either planar or non-planar. In planar devices, all fluxes are parallel to the device surface. The other category comprises membranes and other structures that admit transport from one compartment to another in a direction perpendicular to the device plane.

Several planar technologies today can provide nanochannels with a height smaller than 100 nm. Planar technologies based on classical thin film techniques excel at geometric reproducibility, precision, and scalability through parallel processing of large batches at wafer scale. However, there are

[a] *Biological Micro- and Nanotechnology, Max Planck Institute for Biophysical Chemistry, 37077 Göttingen, Germany. E-mail: tburg@mpibpc.mpg.de*
[b] *Micro System Technology (MST), Centre of Advanced European Studies and Research (caesar), 53175 Bonn, Germany*

† Electronic supplementary information (ESI) available. See DOI: 10.1039/c6lc01089j

This journal is © The Royal Society of Chemistry 2016

Published on 13 October 2016. Downloaded by Stiftung caesar - Bibliothek on 5/12/2020 4:02:52 PM.

limits to the attainable lateral sizes. As the length and width of planar nanochannels are defined by lithography, electron beam lithography is required to go below 1 μm. However, electron beam lithography is relatively slow, expensive, and not well suited for mass production. Either way, the length of planar nanochannels is often constrained by the very practical need to connect to larger feed channels. This generally requires a length greater than a few tens of microns. Therefore, planar nanochannels make excellent devices for precision measurements at the femtoliter scale; but to be able to process macroscopic volumes, extremely expensive large area systems would be needed.

To address this challenge, Fu *et al.* devised a unique silicon process which yields deep lateral trenches of nanoscale width.[13] Although the trenches penetrate deep into the silicon wafer, they are still essentially planar, with all transport occurring parallel to the device surface. The major advantage of the approach is that, by turning the conventional shallow channel design sideways, trenches can be spaced side-by-side at much higher density. However, very precise control over process parameters is required, and the length of the trenches also cannot be shortened below a few tens of microns.

In contrast to planar nanochannels, vertical designs have the capacity to provide fundamentally higher throughput. Perhaps the simplest vertical nanofluidic structures are common filter pores, but their reproducibility and precision does not compare with the extraordinary regularity and exact, arbitrary placement of nanofluidic channels made by lithographic techniques. Thus there is a fundamental trade-off between scalability, permeability, and precision. Unifying these attributes in one and the same device is the holy grail of mesoporous filter technology.

Yet, numerous exciting phenomena can be investigated already, and sometimes advantageously, at the level of single nanopores. High-precision vertical nanopores have been fabricated by a range of top-down nanofabrication technologies, including ion beam sculpting,[14] focused ion beam drilling,[8] e-beam lithography,[15,16] or e-beam drilling in a transmission electron microscope.[17] Controlled dielectric breakdown[18] or track etching[19] have also been adopted, but these provide less control over pore placement and are more difficult to incorporate into standard processes. Although some of these subtractive technologies allow very fine tuning of the open pore area by using feedback,[20] all of them almost inevitably produce shape irregularities and some sidewall roughness, for example due to re-deposition of material or etch defects.

To address this challenge, Desai and colleagues proposed a template-based process for fabricating polysilicon membranes with pore sizes down to a few tens of nanometers using a combination of photolithography, deposition and selective etching.[21] Although this method made it possible to choose the number and location of nanopores and obtain a uniform pore size, to our knowledge, this process has not been shown to be able to yield membranes thinner than 5 μm and the three-dimensional shape of the pores could not be controlled with precision. More recently, Varricchio *et al.* described another impressive technology, which uses nanoscale silicon templates made by electron beam lithography and dry etching to define pores in membranes composed of different layered materials.[22]

In this letter, we describe a new class of nanofluidic devices, which we term vertical nanoslit arrays, that provide both the reproducibly high geometric precision of planar devices and the scalability and throughput of membrane technologies. We also demonstrate the utility of these devices by conducting continuous-flow charge-based filtration of small molecules at a macroscopic scale. Two technological innovations enabled us to implement this concept.

Our first innovation enables the fabrication of vertical nanoslit arrays by combining a new templating method with chemical–mechanical polishing. Templates for the slits are formed by vertical silicon dioxide fins made by the thermal oxidation of single crystal silicon. Therefore, the fin thickness is extremely uniform, and this precision, as well as the smooth finish of the thermal oxide, carry over to the inside of the nanoslits. Chemical–mechanical polishing is employed to planarize the device surface prior to release and to define the final length of the nanoslits in the *z*-dimension.

Our second innovation is to integrate vertical nanoslit arrays in a microfluidic tangential-flow system. Here we demonstrate for the first time that this is effective in eliminating diffusional mass transport limitations on both sides of a submicrometer thick mesoporous membrane.

To characterize the width distribution and defect density of our vertical nanoslit arrays, we performed SEM image analysis, and measurements of ion conductance through membranes with 1 and 12 nanoslits. As an exemplary application, we demonstrated charge-based continuous-flow separation of small molecules with a selectivity of 100 and constant flux over more than 100 hours of operation. Clogging of nanoslits and hindering of the charge selectivity were avoided due to the tangential-flow design and to the high size uniformity and smoothness of the nanoslits walls.

Results and discussion

Fabrication of vertical nanoslit arrays

The main steps of the nanoslit fabrication process are shown in Fig. 1(A). The key step is the generation of 2 μm tall silicon dioxide fins on a silicon wafer as templates for the nanoslits. To create the vertical fins, we first exploit the high crystal-plane selectivity of potassium hydroxide etching to obtain trenches with smooth silicon sidewalls in the <110>-oriented device layer of a silicon-on-insulator (SOI) wafer. A two step alignment scheme is employed to align the trenches with the crystal orientation more accurately than would be possible by the placement of the wafer flats alone;[13,23] the alignment process is described in detail in the ESI.† A thin layer (50 nm) of low-pressure chemical vapor deposited silicon nitride serves as an etch mask.

Published on 13 October 2016. Downloaded by Stiftung caesar - Bibliothek on 5/12/2020 4:02:52 PM.

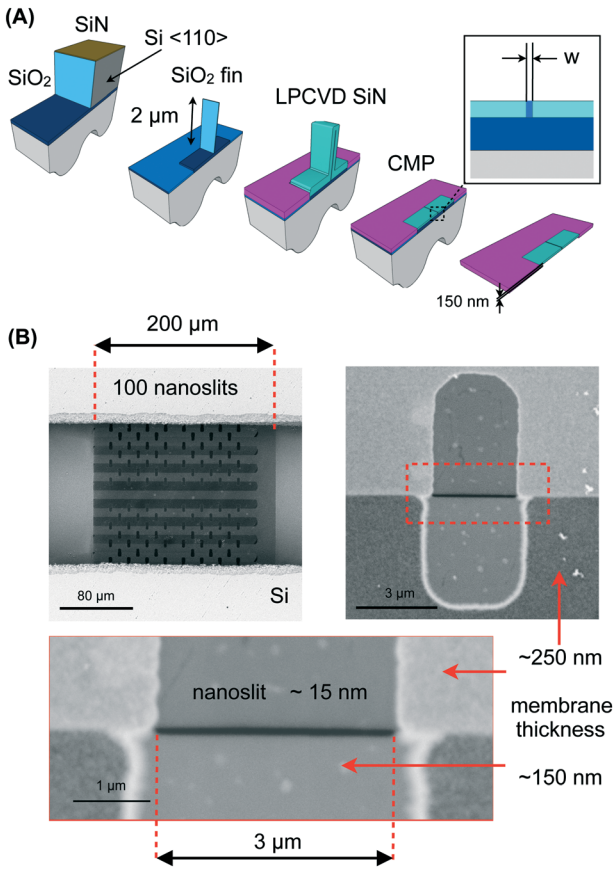

Fig. 1 (A) Main steps of the VNA fabrication process. (B) SEM images of a membrane with 100 nanoslits ~15 nm in width. Different levels of gray represent different thicknesses of the SiN layer resulting from the fabrication procedure (see ESI,† Fig. S1). The nanoslits sit on areas in which the membrane thickness is approximately 100 nm thinner (turquoise area in (A)). This ensure the mechanical stability of a 250 nm thick SiN membrane and the transport properties of a 150 nm thick membrane.

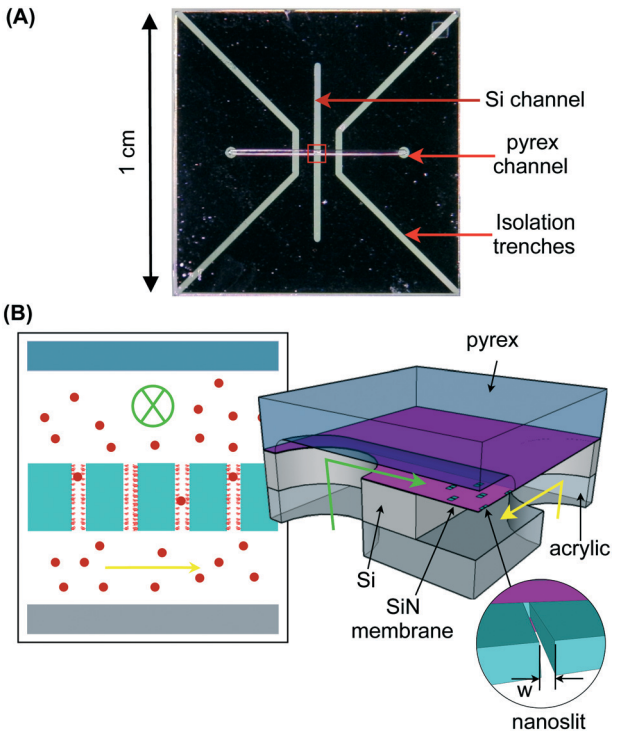

Fig. 2 (A) Optical top view of the microfluidic tangential flow system incorporating the vertical nanoslit array. Two microfluidic channels are crossing above and below the nanoporous membrane. The silicon, which forms the bottom half of the chip is segmented in three electrically insulated parts. (B) Schematic showing the VNA packaged in a tangential-flow microfluidic system.

After etching the trenches, the side walls are thermally oxidized. Thermal oxidation of silicon is among the most uniform, well known and understood methods of thin film growth. Here we exploit this precision to define the fin width in the range from ~15 to 100 nm. The SiN layer that was previously used to mask the KOH etch now protects the wafer surface from oxidation, such that only the vertical walls inside the trenches are exposed.

A sequence of selective wet and dry etches is then used to selectively remove the silicon nitride and the remaining silicon of the SOI device layer, such that only the buried oxide and the vertical fins remain on the wafer surface. Finally, the fins are embedded in a thin conformal layer of LPCVD silicon-rich silicon nitride and the surface is planarized by chemical mechanical polishing. A more detailed description of the fabrication process is reported in the ESI,† Fig. S1.

In order to package the VNA devices in a microfluidic tangential-flow system as shown in Fig. 2, the processed SOI wafer is anodically bonded to a Pyrex wafer in which 6 mm long, 50 μm deep and 200 μm wide channels have already been formed by wet etching using an LPCVD polysilicon mask. The membrane area is defined by bulk micromachining from the wafer backside (see ESI,† Fig. S2). In the last step, the sacrificial oxide is etched selectively by hydrofluoric acid vapor, leaving behind narrow slits which permeate the thin (~150 nm) silicon nitride. Images of a membrane with 100 nanoslits ~15 nm in width are shown in Fig. 1(B).

Nanoslit characterization

SEM analysis. In order to measure the uniformity of the nanoslit width attainable by the new method, we applied an edge-tracking analysis to high-resolution scanning electron microscopy (SEM) images. Our analysis can detect sub-pixel variations in the width of the slits by interpolating the brightness levels and following the position of a fixed contour by a particle-tracking algorithm (see ESI,† Fig. S3).

Fig. 3(B) shows an example of the width distribution obtained by analyzing the images of 12 nanoslits of a membrane chip from a wafer with a final SiO_2 fin thickness of approximately 15 nm. The mean width μ = 15.6 nm and the standard deviation σ = 6 Å, calculated from the width data sets of the 12 slits were used to calculate a Gaussian distribution considered representative of a larger number of nanoslits.

 This journal is © The Royal Society of Chemistry 2016

Published on 13 October 2016. Downloaded by Stiftung caesar - Bibliothek on 5/12/2020 4:02:52 PM.

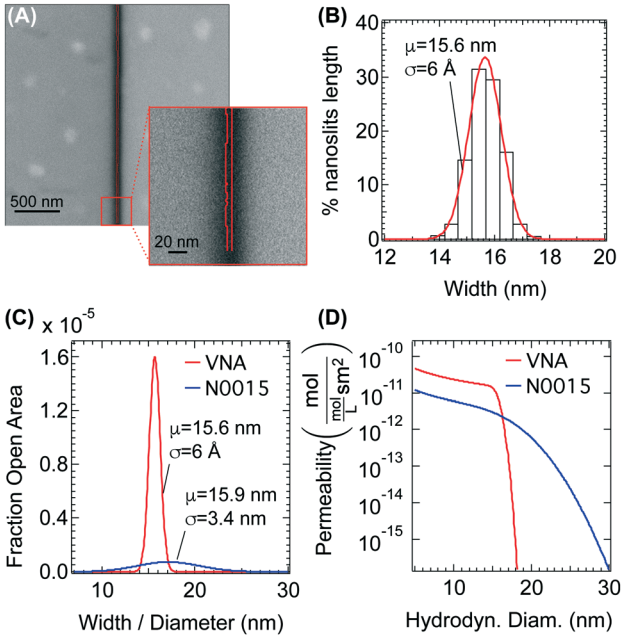

Fig. 3 (A) SEM image analyzed to extract nanoslit edges and widths. (B) The histogram shows the width distribution over the length of 12 nanoslits. The Gaussian distribution with mean μ and variance σ, calculated from the width data set of the 12 slits, here plotted in red, was considered representative of a large number of nanoslits. It should be noticed that both μ and σ can be affected by systematic errors up to 10% resulting from magnification calibration of the SEM. (C) Fraction of open area over a unit of surface area plotted against the slit width of vertical nanoslit arrays VNA (d = 1 × 10^{10} nanoslits per m^2, μ = 15.6 nm, σ = 6 Å) and pore diameter of track etched Nuclepore® N0015 (ref. 24) membranes (d = 6 × 10^{11} pores per m^2, μ = 15.9 nm, σ = 3.4 nm). (D) Comparison of the permeability as a function of the solute hydrodynamic diameter of a unit surface area of VNA and N0015 membranes.

In order to compare vertical nanoslit arrays with track etched membranes, we calculate the theoretical permeability for solutes of different sizes based on the measured pore size distribution. To this end, we first convert the pore size histogram of our 12-slit array to the corresponding fractional open area distributions, as shown in Fig. 3(C). The fractional open area distribution represents the probability density that a point-particle colliding with the membrane passes through a pore or slit of a given width or a given diameter, respectively. Note that the amplitude of the distribution in the case of the vertical nanoslit array (VNA) is two orders of magnitude larger than for the track etched Nucleopore® N0015 membrane. This difference is mainly due to the smaller width of the distribution (σ_{VNA} = 6 Å *vs.* σ_{N0015} = 3.4 nm), as the total open area is of the same order of magnitude. Considering a slit density of 1 × 10^{10} nanoslits per m^2, we obtain a total open area fraction of 0.047% for the VNA and 0.012% (assuming 6 × 10^{11} pores per m^2)[24] for the N0015 membrane. In addition, the nanoslit membrane is forty times thinner than the track etched membrane. These effects conspire to yield a substantially greater permeability of the nanoslit array, as we now show.

We calculated the permeability for diffusional transport as a function of solute hydrodynamic diameter using the following expression:

$$P(X) = \frac{D(X)\int_X^\infty A(x)\mathrm{d}x}{tA_t} \quad (1)$$

where $A(x)$ is the distribution of the open surface area plotted in Fig. 3(C), t is the membrane thickness, A_t is the total membrane area, $D(X)$ the diffusion coefficient, and X is the solute hydrodynamic diameter.

The dependence of the diffusion coefficient on the hydrodynamic diameter is given by

$$D(X) = \frac{k_B T}{3\pi\eta X} \quad (2)$$

where η = 8.9 × 10^{-4} Pa × s^2 denotes the viscosity of water at 25 °C, although this value may be different in strongly confined spaces.

Using the two distributions of open surface area plotted in Fig. 3(C) and the thicknesses t_{VNA} = 150 nm and t_{N0015} = 6 μm, we obtained the permeability of the two membranes, as shown in Fig. 3(D).

Fig. 3(D) reveals a striking improvement in sharpness of the size cutoff when going from the track etched membrane to the vertical nanoslit array. For example, in the track etched N0015 membrane the 'knee' region, over which the permeability drops by a factor of ten, extends to 21 nm, which is 40% above the nominal cutoff. The same attenuation is reached already at 16 nm, or 7%, for the vertical nanoslit array. Stated in another way, solutes 40% larger than the nominal cutoff are only rejected by a factor of ten in the track etched membrane, while the nanoslit array provides six orders of magnitude rejection. It is worth mentioning that such a difference in selectivity is due to an improvement in the pore size distribution by only one order of magnitude.

Conductance measurements. As a first demonstration of the functionality of the system, we measured the ionic conductance G of vertical nanoslit arrays and single vertical nanoslits integrated into a tangential-flow microfluidic system. At the most basic level, this enables us to probe devices for defects and to confirm the average slit width. More importantly, these measurements offer a glimpse of the potential for creating large arrays of identical nanoslits that collectively magnify nanofluidic transport phenomena known from single-pore experiments.

Four point measurements were performed on devices with 1 and 12 vertical nanoslits using a Keithley 2636 SourceMeter connected to the microfluidic device using Ag/AgCl electrodes placed at the inlets and outlets of the microfluidic chip while flowing KCl solutions of equal concentrations in the two crossing channels.

The conductance G was measured at KCl concentrations ranging from 10^{-4} M to 1 M. Although no buffer was used, the pH of all solutions was measured and found to be close

Published on 13 October 2016. Downloaded by Stiftung caesar - Bibliothek on 5/12/2020 4:02:52 PM.

to 5.6. We observed a good repeatability of the measurements over several days of use of the devices, indicating that the nanoslits were not clogging, despite the exposure to highly concentrated KCl solutions which were prepared in a normal laboratory environment and had not been filtered before use.

Fig. 4 shows a log-scale plot of the conductance as a function of the KCl concentration of four membranes from two wafers with different geometries: wafer W_1 with a SiO_2 fin width of ~15 nm, and wafer W_2 with ~25 nm. The conductance shows a linear dependence on concentration in the high electrolyte concentration regime above 10^{-3} M, which is in good agreement with the bulk conductance (dashed lines in the plot) described by

$$G = N\frac{wl}{t}k_b \tag{3}$$

where k_b is the bulk conductivity of a KCl solution at 25 °C, and t is the thickness of the membrane. The concentration dependence is given by k_b, while the magnitude of G changes according to the open area $A = w \times l \times N$ where w is the nanoslit width, l the nanoslit length, and N is the number of nanoslits in the membrane.

A quantitative analysis of the bulk conductance values provides some interesting insights. In the high electrolyte concentration regime, the measurements can be exploited to infer the effective hydrodynamic nanoslit width w when the length l and thickness t are known. In the case of the single-slit devices, we find $w = 15 \pm 3$ nm for W_1, and $w = 27 \pm 3$ nm for W_2, which both are in good agreement with the design values. In the case of the devices with 12 nanoslits, we obtain $w = 17 \pm 2$ nm for W_1, and $w = 24 \pm 2$ nm for W_2 assuming all the nanoslits on the same membrane have the same width.

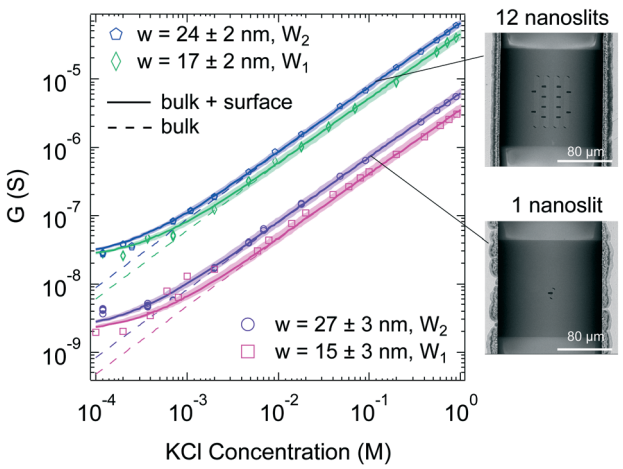

Fig. 4 Ionic conductance measurements on membranes from two different wafers (W_1 and W_2) with 1 and 12 nanoslits. The slit width (w) was determined for each device by fitting the experimental data in the range 1×10^{-2}–1 M with eqn (3). Pearson's r was found larger than 0.84 for all fits. The membrane thickness was 151 ± 5 nm for wafer W_1, and 146 ± 5 nm for wafer W_2. The uncertainty interval is shown as shadow around the curves calculated using eqn (4).

Here our calculations of w are based on parameters for the slit length l and membrane thickness t measured by SEM imaging. We found $l = 3 \pm 0.1$ μm for both wafers, and $t = 151 \pm 5$ nm for W_1 and $t = 146 \pm 5$ nm for W_2, respectively. Note that the thickness t can vary by a few nanometers between chips of the same wafer. As the measurement is destructive, we considered the thickness measured on one chip cross-section as representative for all chips. Therefore differences in the estimated widths for 1-nanoslit devices could be due to differences in the thickness t of the two membranes. Indeed, the uniformity of thermal oxide growth over a wafer surface is much better than the uniformity of the polishing process that determines the membrane thickness.

In the low concentration regime, the conductance of the nanoslits deviates from the bulk behavior, exhibiting strong surface-dominated ionic conductivity between the *cis*- and *trans*-sides of the membrane.[25] The negative surface charge of the silicon nitride slit walls is screened by mobile K^+ counterions that contribute to the overall ionic current. The overall conductance G can be written as

$$G = N\frac{wl}{t}k_b + N\frac{2(w+l)}{t}\mu_K|\sigma| \tag{4}$$

where μ_K is the electrophoretic mobility of potassium, and σ denotes the surface charge density. The first term represents the bulk conductance contribution and the second term the surface conductance contribution. The conductance calculated using eqn (4) with $\sigma = 0.6$ mC m^{-2}, which is compatible with values measured for SiN surfaces at pH 5.6,[26] is plotted for the four devices in Fig. 4 (solid lines). A good agreement between theoretical and experimental behavior is seen in the plot for the four different samples.

An especially interesting result emerges when comparing the transitions from bulk to surface-dominated conductivity between the four membranes. As these transitions are strongly dependent on the slit width, an inhomogeneous or defective array would be expected to show the transition either not at all or at a significantly different electrolyte concentration than the corresponding single slit. However, both the 15 nm and the 27 nm devices begin to deviate from the bulk conductance at approximately 10^{-3} M. Moreover, the conductance values of the 12-slit devices are consistently ~12 times greater than the values for the 1-slit device. This shows that the arrays are free of defects and made up of exact replicas of the single nanoslit to within the accuracy of the measurement.

As a result, very high conductivity values can be achieved by the vertical nanoslits. For example, compared with single-nanopore devices of similar diameter, a single 15 nm wide and 3 μm long slit already conducts 200 times more current at a given *trans*-membrane voltage and electrolyte concentration. The ability to scale this to large arrays without degrading the geometric precision may enable the exploitation of nanofluidic phenomena, such as surface-dominated conductance or gating at a macroscopic scale and without

 This journal is © The Royal Society of Chemistry 2016

Published on 13 October 2016. Downloaded by Stiftung caesar - Bibliothek on 5/12/2020 4:02:52 PM.

sophisticated instrumentation. This would open the path to powerful new applications in sensing, desalination, biotechnological separation, and biomimetics, to name a few.

Continuous separation of charged dyes

The surface-dominated conductance of the vertical nanoslit arrays can be exploited for the continuous separation of molecules by charge. To illustrate this we separated two small organic dyes of opposite charge and similar molecular weight: rhodamine 123 (MW ~ 400, charge +1), and Alexa Fluor 568 (MW ~ 800, charge −3). Due to the presence of anionic silanol groups on the SiN walls of the nanoslits, the anionic Alexa 568 is excluded from the pores by electrostatic repulsion, while the cationic rhodamine 123 is effectively enriched and passes through the membrane. Charge selective transport is a well-known phenomenon seen in planar nanochannels and in vertical nanopores.[19,27] However, the effect is difficult to exploit at macroscopic scale, as mass transport limitations and concentration polarization tend to diminish the rate, and the selectivity is compromised by the heterogeneous pore size distribution in conventional mesoporous membranes.

Vertical nanoslit arrays with tangential flow on both sides overcome this limitation. To see this, we watched for changes in transport rates at different tangential flow velocities and over extended periods of time using two-color fluorescence microscopy. All measurements employed a device from wafer W_2 featuring two 12-nanoslit membranes sharing a common output channel, as shown in Fig. 5(A). A mixture of rhodamine 123 and Alexa Fluor 568 was perfused through two parallel inlet channels (one for each membrane) as shown in Fig. 5(A). DI-water was initially injected into the outlet channel. For efficient use of the sample and to avoid excessive dilution at the outlet, all solutions were pumped back and forth in a reciprocating mode within their respective channels. In contrast, experiments conducted in stopped flow rapidly attained a regime in which the local concentrations on the *cis*- and *trans*-sides of the membrane equilibrated and further transport of molecules was abolished (see ESI,† Fig. S5 and S6).

Fig. 5(B) reveals that the rate of transport for rhodamine 123 is nearly constant during the first hour of the experiment and greatly exceeds the rate of transport for Alexa 568.

By calibrating the fluorescence intensity measurement, we measured fluxes of $3.4 \times 10^8 \pm 0.5 \times 10^8$ molecules per second for the cationic rhodamine dye and $5.6 \times 10^6 \pm 0.5 \times 10^6$ molecules per second for the anionic Alexa 568 dye, corresponding to a selectivity of 100 between the two dyes. Importantly, this value did not decline even after more than 100 hours of running the experiment. In this regard, the sharp cutoff in size and the smoothness of the inner nanoslit walls are extremely beneficial, as all the nanoslits contribute equally to increasing the rate with identical selectivity.

As shown in Fig. 5(C), a minimum flow rate is required to overcome the diffusional transport limitation of molecules from the bulk to the entrance of the nanoslits. The flux of

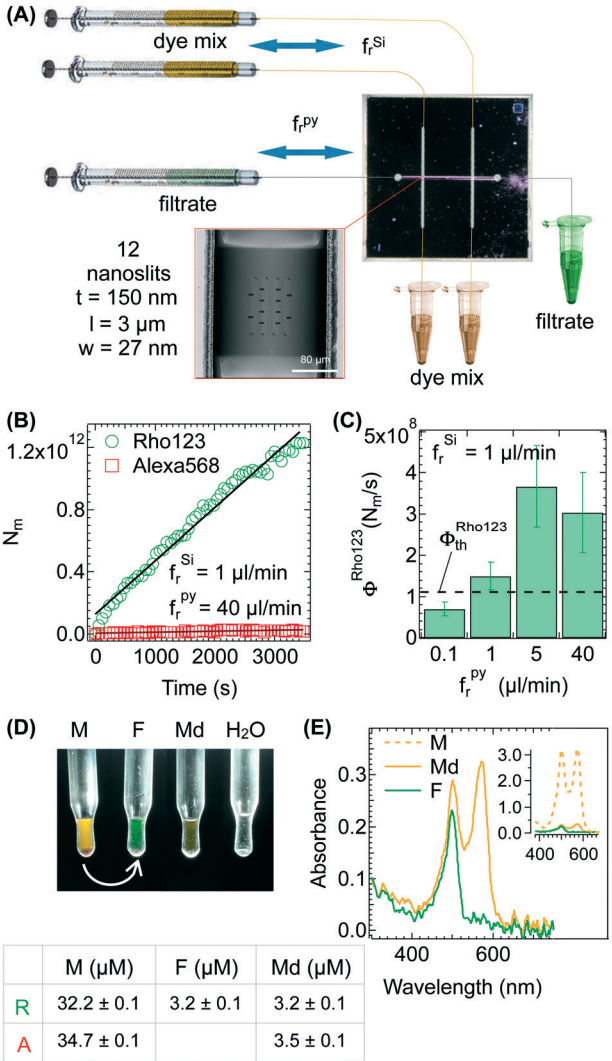

	M (μM)	F (μM)	Md (μM)
R	32.2 ± 0.1	3.2 ± 0.1	3.2 ± 0.1
A	34.7 ± 0.1		3.5 ± 0.1

Fig. 5 (A) Schematic of tangential-flow filtration experimental setup. (B) Plot of the number of molecules (N_m) in the filtrate solution as a function of time. The experiment was performed with a volume of 40 μl of filtrate and dye mix (32.2 μM Rho123, 34.7 μM Alexa 568), flowing at f_r^{py} = 40 μl min^{-1} and f_r^{Si} = 1 μl min^{-1}, respectively. Black straight lines are here used to visualize the average transport rates. (C) Rate of number of molecules of rhodamine per second diffusing into the filtrate for different filtrate flow rates. (D) Vials containing 15 μl of dye mix before filtration (M), filtrate (F), and a 10 times diluted dye mix (Md). (E) Comparison of absorption spectra of the three solutions.

rhodamine 123 increases with the applied flow rate, until a threshold is reached. Only in this regime the transport is completely determined by the geometry and surface charge of the nanoslits.

It has to be pointed out that, the measured flux of rhodamine 123 exceeds the theoretical value of $\Phi_{th}^{Rho123} = 1.1 \times 10^8$ molecules per second calculated using the expression

$$\Phi^{dye} = 2 \times \frac{12 \times (wl)}{t} D_{dye} \Delta C_{dye} \quad (5)$$

for diffusion limited transport through an uncharged nanoslit, assuming $D_{Rho123} = 4.4 \times 10^{-10}$ m^2 s^{-1},[28] and ΔC_{dye} equal

Published on 13 October 2016. Downloaded by Stiftung caesar - Bibliothek on 5/12/2020 4:02:52 PM.

to the initial concentration in the feed solution. A similar value would be expected for Alexa 568 if it was, in fact, able to permeate. This difference is expected due to the exclusion-enrichment effect that gives rise to a depletion of the flux of negative molecules and to an increase of the flux of positive molecules.[27]

The tangential-flow microfluidics allowed us to run the filtration experiments long enough to extract ten percent of the rhodamine 123 dye from the mixed feed solution into the 40 μl filtrate. Fig. 5(D) shows vials containing 15 μl of dye mix (M), filtrate (F) after 117 h of filtration, and a ten times diluted sample of the mixed feed solution (Md) for comparison. Fig. 5(E) shows the absorbance spectra measured to determine the dye concentrations of the three solutions. Using the final concentration to calculate the global flux of rhodamine 123 molecules we obtained an average of $\Phi^{\mathrm{Rho123}} = 1.83 \times 10^8$ molecules per second. This value is comparable to the value extracted by monitoring the fluorescence for a shorter time. The concentration of Alexa 568 in the filtrate solution was below the detection limit of the instrument. This confirms that the selectivity between charged molecules is maintained throughout the filtration process.

It is worth mentioning that in contrast to existing technologies, increasing the filtration rate and the yield in our approach only requires a change in layout, but not in process technology or fabrication time. For example, using vertical nanoslit arrays with 100 instead of 12 slits, only ten hours would be required for the filtration described above, and by increasing the number of feed channels and membranes from two to 100, the time could be shortened to a few minutes.

Conclusions

In conclusion, our results prove the exiting possibility of using vertical nanoslit arrays for exploiting nanofluidic transport phenomena at a macroscopic scale. The technique we developed allows wafer-scale fabrication of vertical nanoslit arrays with Angstrom level uniformity in ultra-thin silicon nitride membranes. Importantly this technique only requires standard procedures established in silicon microtechnology. Efficient solute transport to and from the opening of the nanoslits is provided by incorporating the nanofluidic membrane into a microfluidic tangential-flow system, which also enables continuous operation of the filter chips for several days without clogging. By quantitative analysis of representative SEM images, vertical nanoslit arrays are shown to have a significantly narrower size distribution and larger fractional open area than equivalent track etched membranes. As our resolution was limited by the SEM, the actual slit width distribution may be far sharper than the upper limit obtained by imaging. We show through theoretical analysis that the measured slit width distribution should lead to filter membranes with an unprecedentedly sharp size cutoff. In the future, it will be important to confirm this expectation experimentally; a limiting factor in such experiments may, in fact, become the availability of sufficiently precise, monodisperse, and rigid particles or macromolecules with a hydrodynamic radius on the 10 nm scale. To corroborate our findings from image analysis, we measured the ionic conductivity of single nanoslits and compared the results with nanoslit arrays over a wide range of electrolyte concentration. A clear transition from bulk to surface dominated conduction is observed at the same concentration in both types of devices, and the conductance values agree well with the values expected based on the design. This supports that the arrays are homogeneous and free of defects.

We demonstrated that charge selectivity arising from Debye-layer overlap in the nanoslits can be exploited to achieve continuous tangential-flow separation of similar sized small molecules by charge with an unprecedented selectivity of 100 over more than 100 hours of operation. We envision that the high uniformity, scalability, and microfluidic integration of these membranes will enable a wide range of applications. For example, sensing applications based on monitoring changes in conductivity as target molecules bind inside the slits could be highly sensitive and selective, as membranes with large numbers of slits could simultaneously act as a selective pre-concentration and detection device. Single-molecule detection may also become viable if the fabrication process is augmented with one high-resolution lithography step to shorten the length of the slits to less than 100 nm. In the important application area of molecular separation, our results indicate that vertical nanoslit arrays could enable very high-throughput simultaneous charge and size selective separation of molecules. This principle could also be generalized to other surface dominated mechanisms, such as molecular recognition on bio-functionalized surfaces or active transport by immobilized molecular motors.

Acknowledgements

We thank Prof. Dr. U. B. Kaupp of the Research Center caesar for his generous support, without which this project would not have been possible. Funding for this work was provided by the Max Planck Society and the Max Planck Institute for Biophysical Chemistry, and by the German Ministry for Education and Research under the Biotechnology 2020+ initiative (FKZ 031A159).

References

1 B. M. Venkatesan, B. Dorvel, S. Yemenicioglu, N. Watkins, I. Petrov and R. Bashir, *Adv. Mater.*, 2009, **21**, 2771–2776.
2 K. Venta, G. Shemer, M. Puster, J. A. Rodríguez-Manzo, A. Balan, J. K. Rosenstein, K. Shepard and M. Drndic, *ACS Nano*, 2013, **7**, 4629–4636.
3 V. Dimitrov, U. Mirsaidov, D. Wang, T. Sorsch, W. Mansfield, J. Miner, F. Klemens, R. Cirelli, S. Yemenicioglu and G. Timp, *Nanotechnology*, 2010, **21**, 065502.

 This journal is © The Royal Society of Chemistry 2016

Published on 13 October 2016. Downloaded by Stiftung caesar - Bibliothek on 5/12/2020 4:02:52 PM.

4 M. Tagliazucchi and I. Szleifer, *J. Am. Chem. Soc.*, 2015, **137**, 12539–12551.
5 K. Healy, *Nanomedicine*, 2007, **2**, 459–481.
6 P. Kohli, C. C. Harrell, Z. Cao, R. Gasparac, W. Tan and C. R. Martin, *Science*, 2004, **305**, 984–986.
7 Y. C. Wang, A. L. Stevens and J. Han, *Anal. Chem.*, 2005, **77**, 4293–4299.
8 H. D. Tong, H. V. Jansen, V. J. Gadgil, C. G. Bostan, E. Berenschot, C. J. M. van Rijn and M. Elwenspoek, *Nano Lett.*, 2004, **4**, 283–287.
9 J. Han, J. Fu and R. B. Schoch, *Lab Chip*, 2008, **8**, 23–33.
10 S. J. Kim, S. H. Ko, K. H. Kang and J. Han, *Nat. Nanotechnol.*, 2010, **5**, 297–301.
11 T. Jovanovic-Talisman, J. Tetenbaum-Novatt, A. S. McKenney, A. Zilman, R. Peters, M. P. Rout and B. T. Chait, *Nature*, 2009, **457**, 1023–1027.
12 S. W. Kowalczyk, L. Kapinos, T. R. Blosser, T. Magalhães, P. van Nies, R. Y. H. Lim and C. Dekker, *Nat. Nanotechnol.*, 2011, **6**, 433–438.
13 J. Fu, P. Mao and J. Han, *Nat. Protoc.*, 2009, **4**, 1681–1698.
14 J. Li, D. Stein, C. McMullan, D. Branton, M. J. Aziz and J. A. Golovchenko, *Nature*, 2001, **412**, 166–169.
15 M. M. Deshmukh, D. C. Ralph, M. Thomas and J. Silcox, *Appl. Phys. Lett.*, 1999, **75**, 1631–1633.
16 J. Bai, D. Wang, S. Wook Nam, H. Peng, R. Bruce, L. Gignac, M. Brink, E. Kratschmer, S. Rossnagel, P. Waggoner, K. Reuter, C. Wang, Y. Astier, V. Balagurusamy, B. Luan, Y. Kwark, E. Joseph, M. Guillorn, S. Polonsky, A. Royyuru, S. P. Rao and G. Stolovitzky, *Nanoscale*, 2014, **6**, 8900.
17 A. J. Storm, J. H. Chen, X. S. Ling, H. W. Zandbergen and C. Dekker, *Nat. Mater.*, 2003, **2**, 537–540.
18 R. Tahvildari, E. Beamish, V. Tabard-Cossa and M. Godin, *Lab Chip*, 2015, **15**, 1407–1411.
19 I. Vlassiouk, P. Y. Apel, S. N. Dmitriev, K. Helay and Z. S. Siwy, *Proc. Natl. Acad. Sci. U. S. A.*, 2009, **106**, 21039–21044.
20 E. Beamish, H. Kwok, V. Tabard-Cossa and M. Godin, *Nanotechnology*, 2012, **23**, 405301.
21 T. A. Desai, D. J. Hansford, L. Leoni, M. Essenpreis and M. Ferrari, *Biosens. Bioelectron.*, 2000, **15**, 453–462.
22 S. S. G. Varricchio, H. Cyrille, B. Arnaud and R. Philippe, *Nanoscale*, 2015, **7**, 20451.
23 F.-G. Tseng and K.-C. Chang, *J. Micromech. Microeng.*, 2003, **13**, 47–52.
24 A. Hernández, J. Calvo, P. Prádanos and F. Tejerina, *Colloids Surf., A*, 1998, **138**, 391–401.
25 C. Lee, L. Joly, A. Siria, A.-L. Biance, R. Fulcrand and L. Bocquet, *Nano Lett.*, 2012, **12**, 4037–4044.
26 R. Raiteri, B. Margesin and M. Grattarola, *Sens. Actuators, B*, 1998, **46**, 126–132.
27 A. Plecis, R. B. Schoch and P. Renaud, *Nano Lett.*, 2005, **5**, 1147–1155.
28 P.-O. Gendron, F. Avaltroni and K. J. Wilkinson, *J. Fluoresc.*, 2008, **18**, 1093–1101.